Geophys. J. Int. (2002) **150,** 377–391

Source inversion for estimating the continuous slip distribution on a fault—introduction of Green's functions convolved with a correction function to give moving dislocation effects in subfaults

Haruko Sekiguchi,* Kojiro Irikura and Tomotaka Iwata

Disaster Prevention Research Institute, Kyoto University, Gokasho, Uji, Kyoto 611-0011, *Japan. E-mail: Haruko.Sekiguchi@aist.go.jp*

Accepted 2001 December 14. Received 12 November 2001; in original from 2000 July 4

SUMMARY

In order to obtain knowledge concerning the physics of earthquake rupturing more precisely and to obtain reliable source process for near-source ground motion simulation, we introduced a convolution method that incorporates the effect of a moving dislocation over a rectangular area to a synthetic point source into computing the element source waves for the waveform inversion. Therefore, the rupture directivity effect over the entire fault area is considered fully in the waveform inversion. The rupture process inverted using this technique has a continuous slip distribution inside the subfaults. The moment release history obtained for each subfault directly reflects a slip time function on the subfault because the rupture propagation effect inside each subfault is separated. The validity of this technique is based on the following approximation: the Green's functions from two point sources are approximately the same after a phase correction when the distances between two point sources is much smaller than the distance between the sources and an observation station. The condition for valid usage of this technique has been found through numerical tests. We applied this technique in the waveform inversion of strong motion records for the source process of the 1995 Hyogo-ken Nanbu earthquake. The global characteristics of moment release distributions are similar between two inversion results; one inverted with point-source element waveforms and the other with element source waves considering the finite moving dislocation effects inside each subfault. However, the details are different, e.g. the locations of local maxima of the total moment release are different between these inversion results. A positive correlation between final slip and peak slip velocity is observed.

Key words: earthquakes, faulting, fault slip, rupture propagation.

1 INTRODUCTION

Usually, a source fault in the waveform inversion used to be represented by a set of point sources placed at several kilometre intervals on planar surfaces. Such techniques have the following problems.

(1) Each point source is assumed to represent a sum of moments released around it. The rupture directivity from the total source is realized by overlapping of waves from an aggregate of the point sources. However, a wave from each of the point sources does not include the rupture directivity effect itself. Therefore, the amplitudes of the waves from the entire source area in the forward directivity region are underestimated. And in contrast, those in the backward directivity region are overestimated (Fig. 1, left). The rupture directivity effect is caused by coherent overlapping of waves. It is expected that coherent overlapping of waves be gradually suppressed as the frequency content of the waves become higher because of the heterogeneity of the wave propagation and rupture process. Somerville *et al.* (1997) showed this phenomenon in observations in the near-source area. They showed that the rupture directivity effect is remarkable for periods longer than 0.6 s. The frequency range of our waveform inversion is 0.1–1.0 Hz, where the directivity effect might be strongest according to Somerville *et al.* (1997). Using element waves with no rupture propagation inside the subfaults in the waveform inversion, misestimation of the moment release values may happen depending on the distribution of the observation stations.

(2) The moment release history obtained for each point source includes both a slip time function and a rupture propagation effect inside each subfault. It is impossible to separate them because rupture propagation inside each subfault is not defined. However, the quality of the estimated slip time functions determines the quality of the dynamic rupture model parameters estimated in the study of

*Now at: Active Fault Research Center, Geological Survey of Japan, AIST (National Institute of Advanced Industrial Science and Technology), Site 7, 1-1-1 Higashi, Tsukuba, 305-8567, Japan.

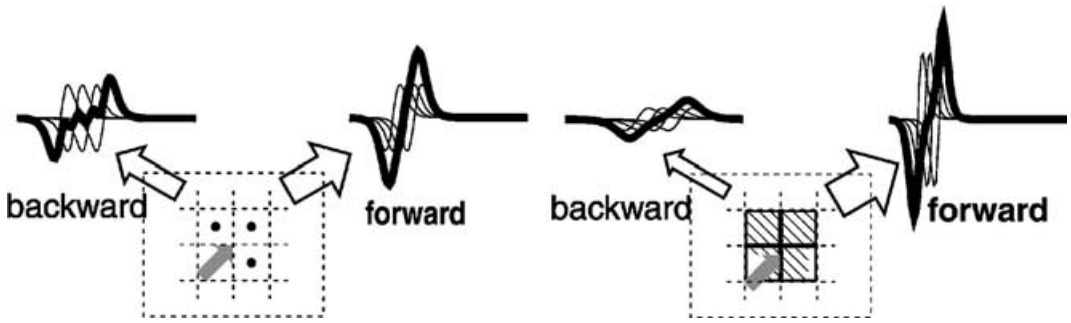

Figure 1. Schematic explanation of the difference in the rupture directivity effect expected to appear in the waveforms between those caused by with (right) and without (left) considering rupture propagation inside each element source area.

the dynamic rupture of real earthquakes (e.g. Guatteri & Spudich 2000).

(3) Recently, total wavefield modelling considering both the source process and wave propagation in realistic 3-D structure has been performed in order to understand the mechanisms of ground motion generation and further to make reliable ground motion predictions for future earthquakes. If a source model represented by sparsely distributed point sources is used as an input to such ground motion simulations, the highly concentrated sources near the surface of the earth can generate artificial, large ground motion around themselves. If slips are interpolated to obtain a smooth distribution from a source model represented by sparsely distributed point sources, the smoothed slip distribution never generates the ground motion that the original source model does but generates its high-cut off motion.

Therefore, it is desirable to take into account rupture propagation inside each subfault in the waveform inversion. To simulate the effect of rupture directivity on each subfault, Wald & Heaton (1994) and Wald, Heaton & Hudnut (1996) calculated synthetic waves from many point sources over each subfault (25 point sources in Wald 1996) and summed them up considering rupture time delays (hereafter 'summation method' and simply indicated as SM). An interpolation technique was used in their work to reduce the amount of computation needed for the Green's functions.

In the present study, by convolving a function representing a bi-directional moving dislocation on each subfault with the point-source synthetic wave from each subfault centre (hereafter called the 'convolution method' and simply indicated as CM), we obtain an approximate synthetic wave from a uniformly distributed slip inside the subfault activated successively by a triggering front propagating in an arbitrary direction (Fig. 1, right).

The representation of a moving dislocation effect in convolutional form was first formulated by Ben-Menahem (1961). He evaluated Love and Rayleigh waves from a finite moving source and showed that source dimension and rupture propagation velocity play important roles in radiation pattern when the size of the source becomes of the order of the dominant wavelength of radiated waves. He applied this idea to body waves in Ben-Menahem (1962). Aki (1968) added a unidirectional moving dislocation effect to gridpoint sources using this method in forward modelling of the observed waveforms recorded at 80 m distance from the causative fault during the 1960 Parkfield earthquake. Analytical expressions of the radiation field from a propagating source with spatially heterogeneous slip distribution were proposed by Ben-Menahem & Singh (1981, pp. 230–244). Their formulation is not practically useful for problems like ours where we investigate complicated heterogeneity of source processes using near-source ground motion records. First, because their formulation requires an extreme simplification of the source process to make the analytical integration possible. And secondly, because Ben-Menahem and Singh's formulation assumes that Green's functions from points over a fault plane are the same except for phase shifts, which is usually an impossible assumption.

First, we seek a condition to validate the usage of this technique, which can be found through numerical tests. Next, we apply this technique to the waveform inversion of strong motion records for the source process of the 1995 Hyogo-ken Nanbu earthquake. The inverted rupture process using the element source waves by CM has a continuous slip distribution inside each subfault. The obtained moment release time history on a subfault directly reflects the slip time function at any point on the subfault. Such a model, used as an input for the near-source ground motion simulation, avoids the problem of artificial, large ground motions around the point sources owing to the use of sparsely distributed point sources. We use the same fault plane model and the same data set as those in Sekiguchi *et al.* (2000) and used part of their result (the local rupture velocity vectors and the trigger time of subfaults). Sekiguchi *et al.* (2000) inverted strong motion records. They carefully located a multiple-segment fault plane model considering the geodetic data and particle ground motions near the estimated causative fault, and used many near-source stations. We expect details of the source process to be well constrained in their source model.

2 METHOD

2.1 A moving dislocation inside subfaults by convolution in homogeneous media

The representation of a moving dislocation effect in the convolutional form in a homogeneous media is deduced as follows (modified from Sato 1969). We consider a rectangular subfault (Σ) of length L and width W on the $\xi_1\xi_2$-plane, dislocations parallel to the plane are uniformly distributed inside the subfault and a propagating rupture on it. A displacement field from this extended source is

$$\begin{aligned} U_n(\mathbf{x}, t) &= \int\int_{\Sigma} m_{pq}(\boldsymbol{\xi}, \tau) * G_{np,q}(\mathbf{x}, t; \boldsymbol{\xi}, \tau)\, d\boldsymbol{\xi} \\ &= \int\int_{\Sigma} \sum\nolimits_{p=\xi_1,\xi_2} m_{p\xi_3}(\xi_1, \xi_2, \tau) * G_{np,\xi_3}(\mathbf{x}, t; \xi_1, \xi_2, \tau)\, d\xi_1\, d\xi_2 \end{aligned} \tag{1}$$

where $m_{pq}(\xi, \tau)$ is the moment density tensor representing dislocation in the p-direction on a plane normal to the q-direction at a

position $\boldsymbol{\xi}$, and $G_{np,q}(\mathbf{x}, t; \xi, \tau)$ is a spatial derivative of the Green's tensor representing the nth component of a displacement response at a point $\mathbf{x}$ to the impulse source $m_{pq}(\xi, \tau)$. When the following two conditions are satisfied, the Green's function from an arbitrary point on the subfault to the station approximates to that from the reference point after correcting for the time delay owing to the difference of location (hereafter, we call this the 'plane-wave approximation'). The conditions are: (1) the extension of the subfault is much smaller than the distance between a reference point (the centre of the subfault) and (2) a station, and second (higher-) order microterms in the difference of two distances; one between the reference point ($(\xi_1, \xi_2) = (0, 0)$) and a station and the other between an arbitrary point on the subfault and the station, is negligible.

$$G_{np,q}(\mathbf{x}, t; \boldsymbol{\xi}, \tau) \cong G_{np,q}(\mathbf{x}, t - t_{\mathrm{d}}; \mathbf{0}, \tau), \tag{2}$$

$$t_{\mathrm{d}} = \frac{1}{c}\left(\frac{\boldsymbol{\xi}\mathbf{x}}{R}\right) = \frac{1}{c}\left(\frac{\xi_1 x_1 + \xi_2 x_2}{R_{\xi_1\xi_2}}\right)$$

where (x_1, x_2) is a station location in the subfault coordinate, $R_{\xi_1\xi_2}$ is the distance between the reference point and the station projected on to the $\xi_1\xi_2$-plane ($R_{\xi_1\xi_2} = \sqrt{x_1^2 + x_2^2}$), c denotes the P- or S-wave velocities (V_P and V_S) at the source location. The condition to be satisfied for the plane-wave approximation is the same as that for the region of Fraunhofer diffraction in optics (Aki & Richards 1980),

$$l^2 \ll \frac{\lambda R}{2} \tag{3}$$

where l, λ and R are the linear dimension of the source area, the wavelength and the distance between a receiver and the source, respectively. We assume a common moment release function (i.e. a common mechanism and time history) over a subfault with length L and width W, and linear rupture front propagation whose velocities in the ξ_1 and ξ_2 directions are V_{r_1} and V_{r_2}, respectively, then,

$$m_{p\xi_3}(\xi_1, \xi_2, \tau)\big|_{p=\xi_1,\xi_2} = m_{0p\xi_3}\left(0, 0, \tau - \frac{\xi_1}{V_{r_1}} - \frac{\xi_2}{V_{r_2}}\right)\Bigg|_{p=\xi_1,\xi_2}. \tag{4}$$

Substituting eq. (2) for the S-wave part (the direct S-wave is dominant in the waveform inversion) and eq. (4) into eq. (1), we obtain,

$$U_n(\mathbf{x}, t) = \sum_{p=\xi_1,\xi_2}\left\{\int\!\!\int_{\Sigma} m_{0p\xi_3}\left(0, 0, \tau - \frac{\xi_1}{V_{r_1}} - \frac{\xi_2}{V_{r_2}}\right) * G_{np,\xi_3} \times \left(\mathbf{x}, t - \frac{1}{V_S}\left(\frac{\xi_1 x_1}{R_{\xi_1\xi_2}} + \frac{\xi_2 x_2}{R_{\xi_1\xi_2}}\right); 0, 0, \tau\right) d\xi_1\, d\xi_2\right\}. \tag{5}$$

Taking a Fourier transform of both sides of the above formula,

$$U_n(\mathbf{x}, \omega) = \sum_{p=\xi_1,\xi_2} m_{0p\xi_3}(0, 0, \omega) G_{np,\xi_3}(0, 0, \omega) L W \frac{\sin X_S}{X_S}\frac{\sin Y_S}{Y_S} \tag{6}$$

with

$$X_S = \frac{\omega L}{2V_S}\left(\frac{V_S}{V_{r_1}} - \frac{x_1}{R_{\xi_1\xi_2}}\right) \quad Y_S = \frac{\omega W}{2V_S}\left(\frac{V_S}{V_{r_2}} - \frac{x_2}{R_{\xi_1\xi_2}}\right). \tag{7}$$

From eq. (6) it is understood that the displacement field from a rectangular finite moving dislocation is obtained by convolving the Green's function with a common moment density function and a 'finite moving dislocation function',

$$\frac{\sin X_S}{X_S}\frac{\sin Y_S}{Y_S}. \tag{8}$$

We can extend the above formulae to a case of a heterogeneous media by changing t_{d} in eq. (2) to

$$t_{\mathrm{d}} = \frac{1}{V_S}(\xi_1 r_{01} + \xi_2 r_{02}), \tag{9}$$

where $\mathbf{r}_0 = (r_{01}, r_{02})$ is the takeoff vector of a ray on the $\xi_1\xi_2$-plane at the source. Then eq. (7) becomes

$$X_S = \frac{\omega L}{2V_S}\left(\frac{V_S}{V r_1} - r_{01}\right), \quad Y_S = \frac{\omega W}{2V_S}\left(\frac{V_S}{V r_2} - r_{02}\right). \tag{10}$$

Practically, we perform ray tracing to obtain the takeoff vector of the direct S-wave ray for each subfault–station pair.

2.2 Validity and limitations of the convolution method

As we saw in the previous section, the applicability of CM is based on the plane-wave approximation assumption. The Fraunhofer inequality condition (eq. 3) is qualitative and cannot be used to estimate the approximation error expected for a given set of (L, λ, R). We assume that the right-hand side of the Fraunhofer inequality divided by the left-hand side,

$$C_{\mathrm{fraun}} = \frac{\lambda R}{2L^2} \tag{11}$$

with

$$V_S\left(t_0 + \frac{L}{V_{r_1}} - \frac{L}{V_S}\right) \lesssim \lambda \lesssim V_S\left(t_0 + \frac{L}{V_{r_1}} + \frac{L}{V_S}\right),$$

works as an index to predict the approximation error, and try to find a critical value to give sufficiently small errors for the numerical tests. t_0 is the rise time and V_r is the rupture propagation velocity.

The approximation error depends on the takeoff vector of the direct S-wave ray ($\mathbf{r}$) and on the distance R between the centre of the subfault and a station, of source size L and wavelength λ, because the effective source extensions seen from stations vary with the takeoff vectors. When rupture propagation inside the subfault is considered, the amount of error also depends on the rupture propagation direction (measured as the angle, λ, between the rupture propagation direction and the subfault strike) and velocity (V_r). We search for a condition to give a quantitative error estimation required for the plane-wave approximation combined with the moving dislocation in the following process.

We (1) search a condition of $(\mathbf{r}, \lambda, V_r)$ to give the maximum error for fixed (L, R) and $W = L$; (2) examine how the approximation error varies with R for fixed L and the 'worst set' of $(\mathbf{r}, \lambda, V_r)$ found in (1), determine the value of R to give a 10 per cent error as the critical distance for the corresponding L, determine $C_{\mathrm{fraun,critical}}$ corresponding to a 10 per cent error; and (3) examine the change of error when L and R varies, keeping $C_{\mathrm{fraun,critical}}$ for a fixed $(\mathbf{r}, \lambda, V_r)$.

In the following numerical tests, we calculate target waveforms to be compared with waveforms by CM using SM with a sufficient number of point sources. The accuracy of the numerical integration increases as the discretization interval become small. We found that a point-source interval of about 400 m is enough to realize the directivity effect well in the frequency range 0.1–1.0 Hz, which is the frequency band for the present waveform inversion study. The rise time is fixed at 0.6 s and the S-wave velocity (V_S) is set to 4.33 km s^{-1}.

The subfault is square in shape. The approximation errors are measured with misfits between the waveforms by CM and those

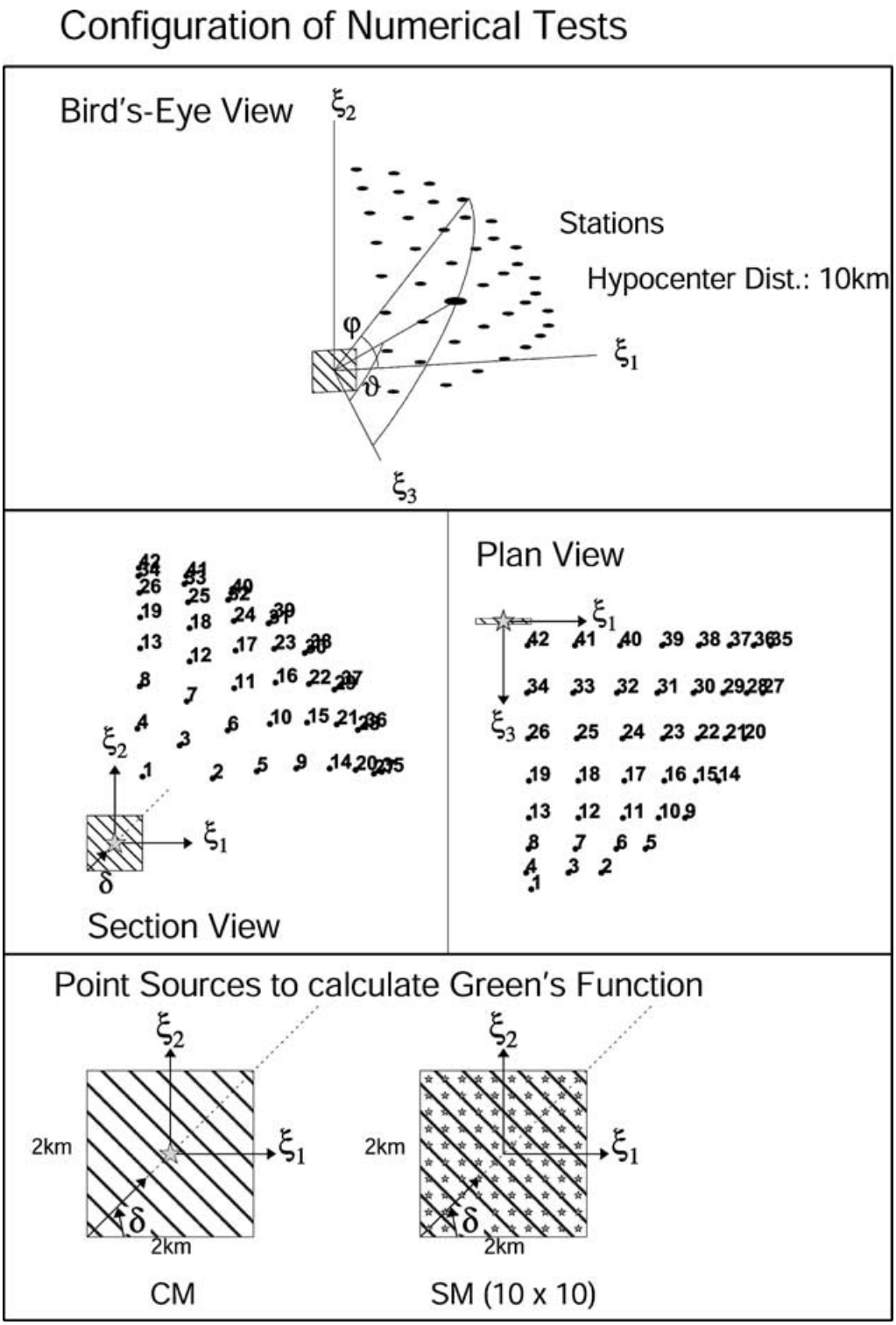

Figure 2. Configuration of the numerical tests for examining the validity and limitation of CM. The ξ_1 and ξ_3 directions correspond to north and east directions in the following figures (from Figs 3–5), respectively.

by SM. The misfit is defined as the summation of square residuals between the two waveforms divided by the maximum of the three components of the summation of the square amplitudes of the target waveforms,

$$\text{misfit}_{jcmp} = \frac{\int (d_{\text{SM}jcmp} - d_{\text{CM}jcmp})^2\, dt}{\max_{icmp=1,2,3} \left\{ \int d^2_{\text{SM}icmp}\, dt \right\}}, \tag{12}$$

because in our waveform inversion observed and synthetic waveforms at each station are normalized to the maximum amplitude of the three components of the observation.

In the first step of the numerical test, we fixed $L = 2$ km, $R =$ 10 km, and the rake of the slip vector $= 180^\circ$. Varying V_r from 50 to 100 per cent of V_S, and δ from 0° to 360°, the waveforms at stations in various directions $\mathbf{r}$ (denoted by ϑ and φ) are calculated

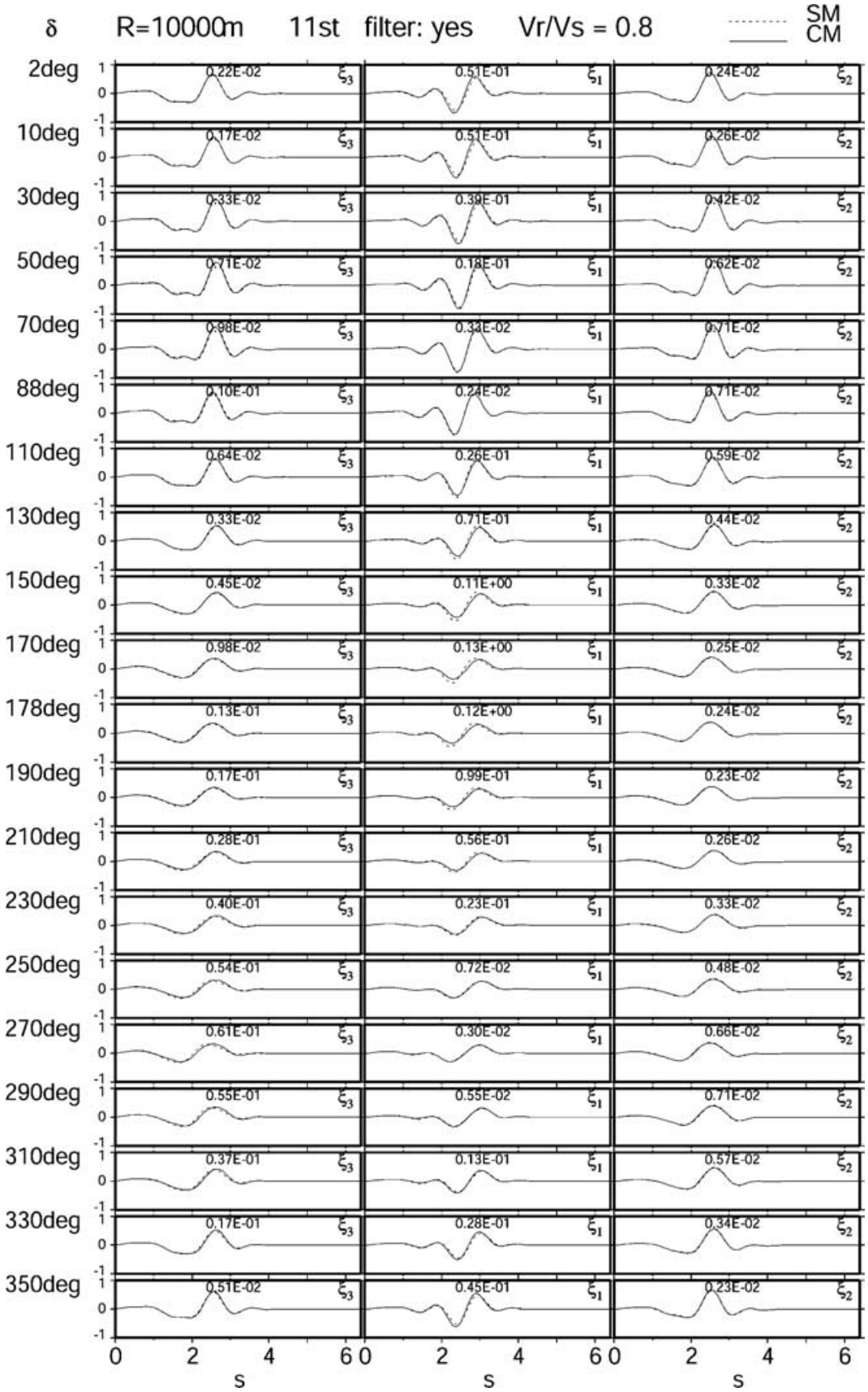

Figure 3. Synthetic velocity waveforms using CM (solid lines) and SM (dashed lines) for the half-space velocity structure. All the synthetics are bandpass filtered in the range 0.1–1.0 Hz.

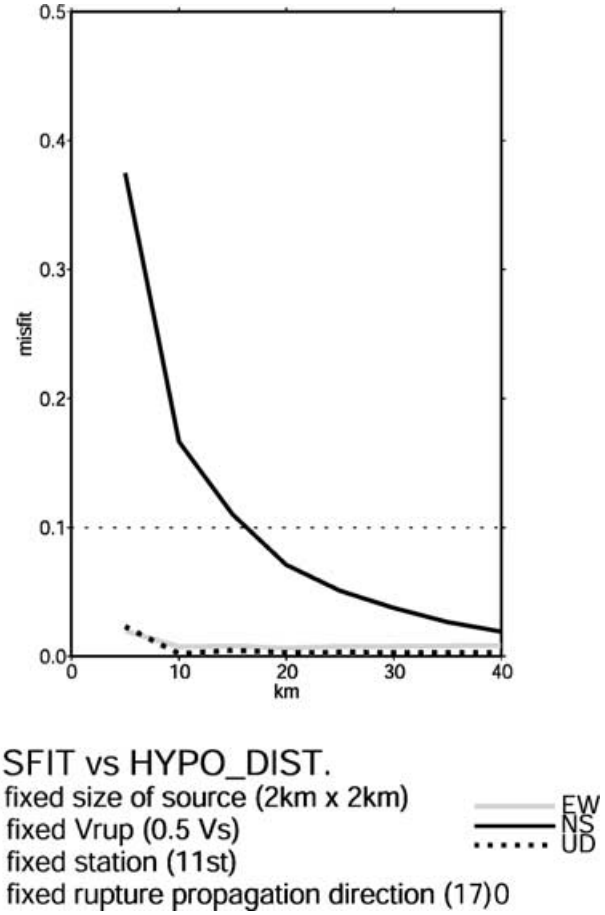

Figure 4. Variation of the approximation error (misfit) against the hypocentre distance fixing the rupture velocity, rupture propagation direction, takeoff angle and subfault size to the 'worst set'; $V_r = 0.5V_S$, $\delta = 170^\circ$, station no 11 $(\vartheta, \varphi) = (45^\circ, 52.5^\circ)$.

using both CM and SM (Fig. 2). The stations are distributed at about every 10° in ϑ and φ. Varying δ, ϑ and φ within these ranges, all possible combinations of subfault plane orientation, slip direction and station direction are covered in a discrete manner. Examples of the waveforms from both methods for one V_r and one $\mathbf{r}$ and for various δ are shown in Fig. 3. The misfit is largest when V_r is smallest in the range we tested, δ is around 170°–180°, and in the direction of station no 11. Here, we neglected the cases where the takeoff vector is in the nodal direction for the radiation pattern of the corresponding component (less than 10 per cent of the maximum radiation).

In the second step, we calculated the waveforms fixing $L =$ 2.0 km and the 'worst set' of $(\mathbf{r}, \lambda, V_r)$; $\delta = 170^\circ$, $V_r = 0.5V_S$, station no 11 ($\vartheta = 45^\circ$ and $\varphi = 52.5^\circ$), and varying $R =$ 5–40 km. The misfit decays almost proportionally to the inverse of R, and has a 10 per cent error (misfit $= 0.1$) at $R = 16.3$ km (Fig. 4). We call this distance the critical distance for $L = 2.0$ km. The C_{fraun} value for the condition of the critical distance was 17.4, values for several other plane-wave approximation error levels are listed in Table 1.

In the third step, to assess whether C_{fraun} can be an index to evaluate errors in a waveform by CM originating from the plane-wave approximation, we examined the variation of misfit for fixed $(\mathbf{r}, \delta, V_r)$, when L and R are varied while keeping $C_{\text{fraun}} = 13.6$, which is the value at the critical distance for $L = 2.0$ km. The misfits kept constant for larger distances, as we had expected (Fig. 5). However, for smaller distances, the misfits were smaller than those expected from C_{fraun}. This is because the wavelength corresponding to the predominant frequency of the filtered waveform is larger than the characteristic wavelength evaluated from L. Effectively, C_{fraun} becomes larger than 13.6. From these results, it is confirmed that C_{fraun} is useful for estimating the maximum error from the plane-wave approximation for any hypocentre distance and subfault size. By calculating the C_{fraun} value, we can judge whether only one Green's function from a reference point inside a subfault to a station is enough to approximate a path effect between any point inside the subfault and the station. If the subfault–station distance is smaller than the critical distance for a given subfault size from the viewpoint of C_{fraun}, we need to subdivide the subfault into smaller pieces so that the piece size satisfies the condition $C_{\text{fraun}} > C_{\text{fraun,critical}}$. Then we can apply CM for every piece.

Table 1. List of C_{fraun} values corresponding to different levels of plane-wave approximation error.

Max. plane-wave approximation error	0.05	0.1	0.2
C_{fraun}	26.7	17.4	9.6

Table 2. Parameters of the fault model.

Active fault		Strike (deg)	Dip (deg)	Length (km)
Segment A	Nojima	45.0	78.0	20.5
Segment B	Suma	50.0	90.0	14.35
Segment C	Suwayama	233.0	82.0	10.25
Segment D	Gosukebashi	218.0	82.0	12.3
Segment E	Okamoto	268.0	82.0	6.15

Table 3. Observed seismograms used in this analysis.

Station	Lat.	Lon.	Organization
AMC	34.7180	135.4080	CEORKA
CHY	34.4390	135.6590	CEORKA
KBU	34.7250	135.2400	CEORKA
MOT	34.7250	135.2810	CEORKA
TDO	34.4800	135.4080	CEORKA
TOY	34.8010	135.5010	CEORKA
AID	34.940	134.168	JMA
AIO	33.792	134.452	JMA
AWA	34.336	134.908	JMA
HEG	34.653	135.685	JMA
KOB	34.69	135.18	JMA
KOY	34.218	135.593	JMA
MRT	33.2483	134.1800	JMA
OKA	34.6583	133.9183	JMA
OSA	34.6783	135.5217	JMA
WAC	35.283	135.402	JMA
NKY	34.9667	135.6222	Kansai Electric Power Co. Inc.
SOK	34.7431	135.4417	Kansai Electric Power Co. Inc.
KMT	34.383	135.35	RRI, Kyoto Univ.
ABU	34.8600	135.5735	RCEP DPRI, Kyoto Univ.
KN1	34.855	135.217	Matsumuragumi Co. Inc.
NRT	34.234	134.641	Honshu-Shikoku Bridge Public Corporation
TZK	34.8083	135.3437	Railway Technical Research Institute
RKI	34.6883	135.2728	Sekisui House Co. Inc.
KPI	34.670	135.208	Kobe City

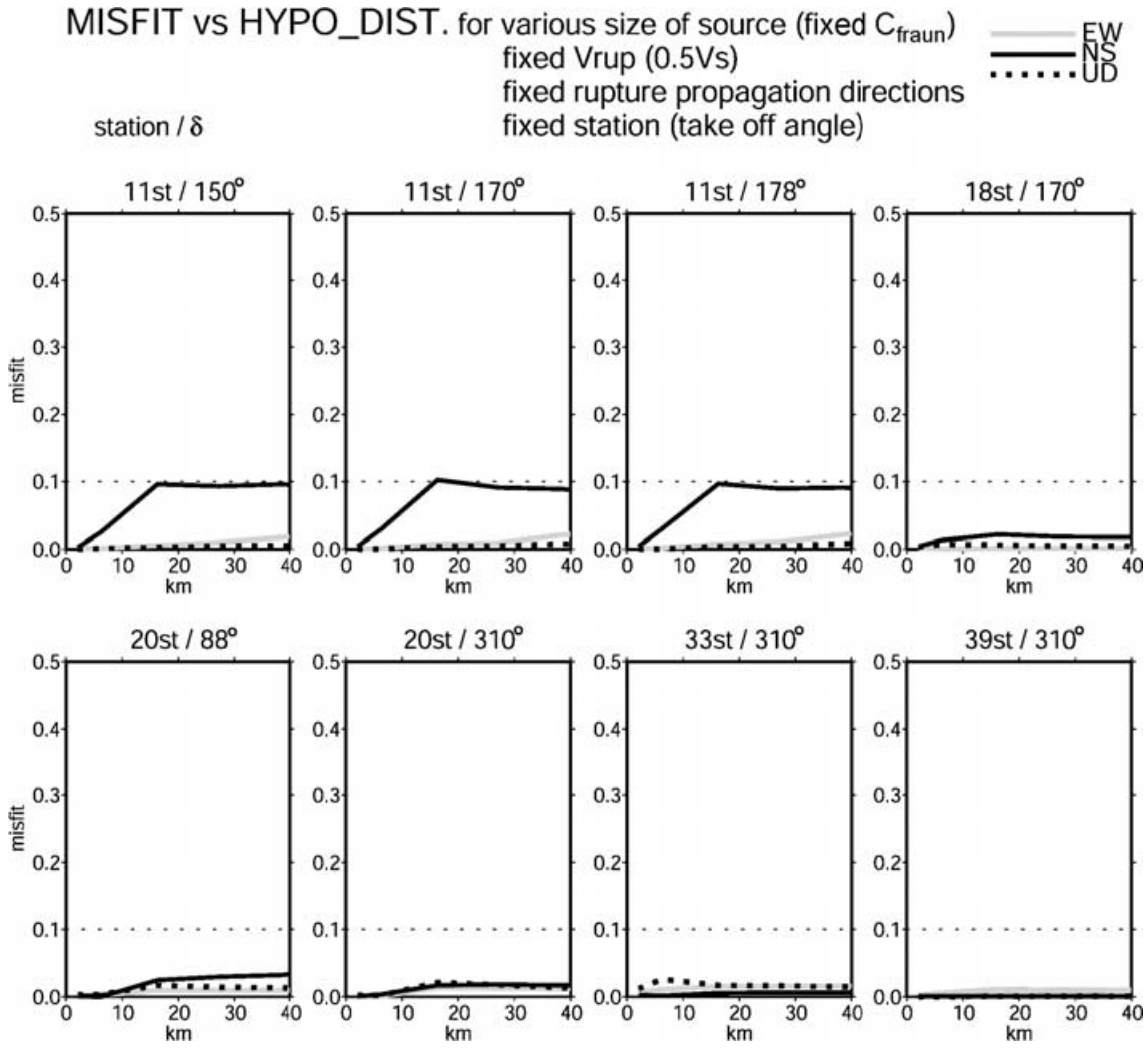

Figure 5. Variation of misfit against the hypocentre distance fixing rupture velocity, rupture propagation direction, takeoff angle and varying the subfault size and hypocentre distance so that the C_{fraun} value stays constant.

3 APPLICATION TO THE WAVEFORM INVERSION

3.1 Preparation of element source waveforms including rupture propagation inside each subfault for the waveform inversion

On introducing CM to the calculation of element source waveforms for the waveform inversion, we make the following operation to satisfy the applicability condition examined in the previous section (Fig. 6).

After locating the model fault planes and discretizing them into small subfaults, we calculate the distances between every subfault–station pair. If the distance between a pair is larger than the critical distance to give a certain level of maximum error for a given subfault size, we calculate one Green's function between the centre of the subfault and the station, and convolve it with the 'finite moving dislocation function' and the element slip time function (eq. 6). If the distance is smaller than the critical subfault–station distance, we calculate the critical source size to satisfy $C_{\text{fraun}} > C_{\text{fraun,critical}}$ for that distance. We subdivide the subfault into smaller pieces so that the size of the pieces is smaller than the critical source size, calculate the Green's functions between the point sources on all the pieces and the station, convolve them with the 'finite moving dislocation function' and the element slip time function. Then we sum them up considering the rupture time delays to obtain one element source waveform for one subfault. We can rewrite eq. (6) when subdividing of a subfault into smaller pieces is required:

$$U_n(\mathbf{x},\omega) = \sum_{i=1}^{N_S^2} \sum_{p=\xi_1,\xi_2} \left[m_{0\xi_3}(0,0,\omega) * G_{np,\xi_3}(\xi_{0_i1}, \xi_{0_i2}, \omega) \times \frac{LW}{N_S^2} \frac{\sin X_{S_i}}{X_{S_i}} \frac{\sin Y_{S_i}}{Y_{S_i}} \exp\left(i\omega \frac{\xi_{0_i1}}{V_{r_1}} + i\omega \frac{\xi_{0_i2}}{V_{r_2}} \right) \right], \tag{13}$$

with

$$X_{S_i} = \frac{\omega L}{2V_S N_S} \left(\frac{V_S}{V_{r_1}} - r_{0_i1} \right), \quad Y_{S_i} = \frac{\omega W}{2V_S N_S} \left(\frac{V_S}{V_{r_2}} - r_{0_i2} \right), \tag{14}$$

where N_S^2 is the number of the subdivision required. (ξ_{0_i1}, ξ_{0_i2}) is the coordinate of the centre of the ith piece and $\mathbf{r}_0$ is a takeoff vector of the ray in the $\xi_1\xi_2$-plane at (ξ_{0_i1}, ξ_{0_i2}).

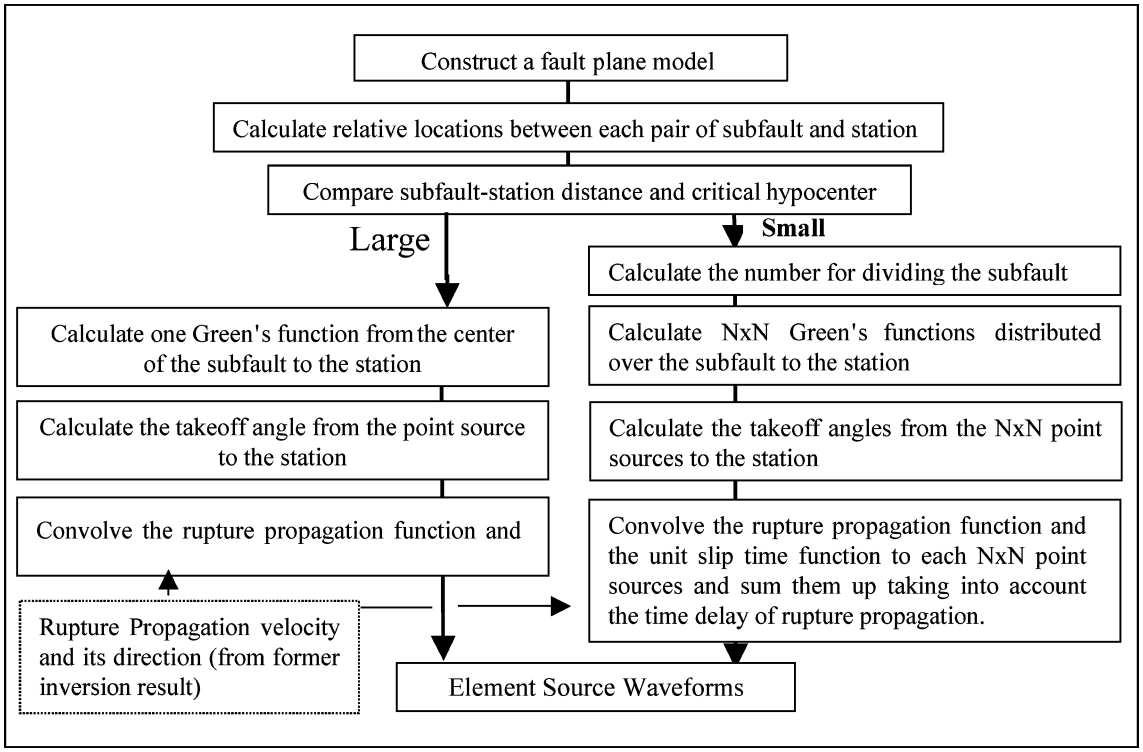

Figure 6. Flow chart for calculation of the element waveforms with a finite moving dislocation effect for the waveform inversion.

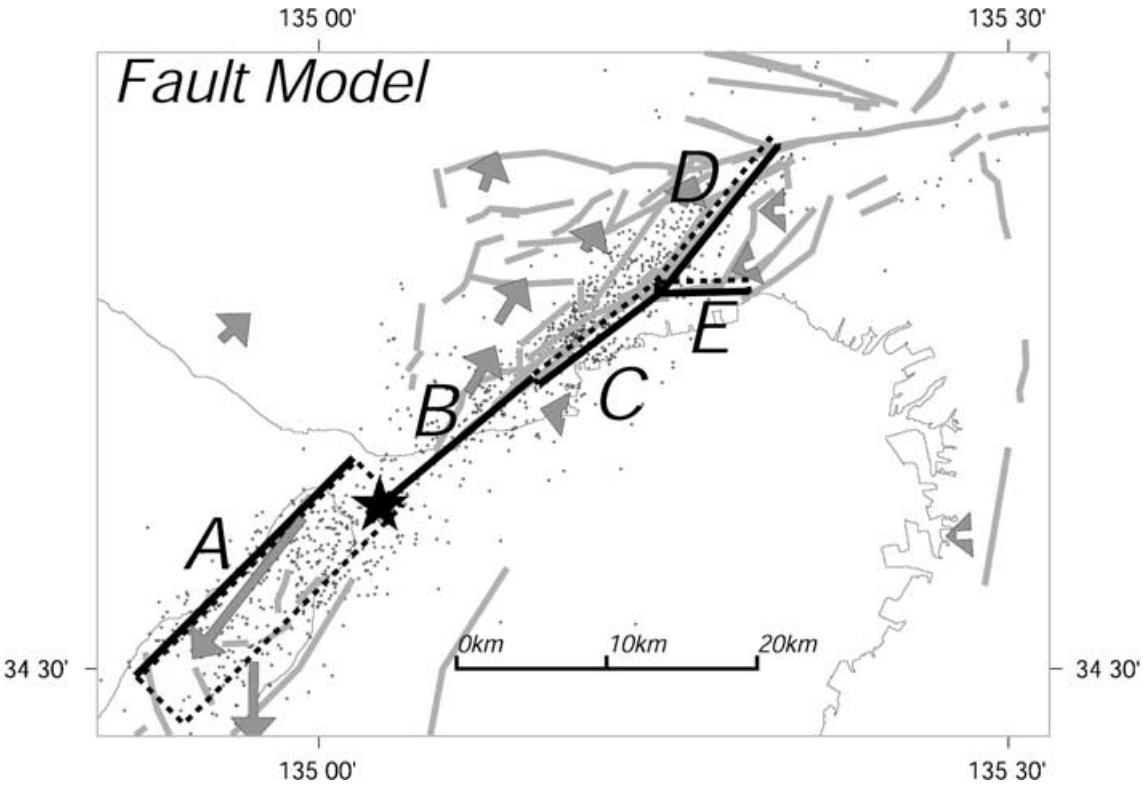

Figure 7. Fault plane model for the waveform inversion for the source process of the 1995 Hyogo-ken Nanbu earthquake. Black and grey lines show the active fault traces from Ishihara *et al.* (1991). The black lines are those estimated to be causative faults in Sekiguchi *et al.* (2000) and in this study. Epicentres of the main shock and aftershock during the day of the main shock occurrence are determined by Nemoto *et al.* (1996, 1997). Circles represent the epicentres of aftershocks 18 h after the main shock. Vectors show static displacements during 1984 and 1995 after the earthquake, as determined by Hashimoto *et al.* (1996) from GPS data.

3.2 Application to the source inversion of the 1995 Hyogo-ken Nanbu (Kobe) earthquake

We apply CM in the waveform inversion for the source process of the 1995 Hyogo-ken Nanbu earthquake ($M_{JMA} = 7.2$, 05:46:51.5 JST, 17 January 1995, latitude 34.598, longitude 135.044, depth 16.37 km) hypocentre location information by Nemoto *et al.* (1997). We use the same fault plane model (Fig. 7 and Table 2) and the same data set (Fig. 8 and Table 3) as that in Sekiguchi *et al.* (2000), taking into account the surface rupture trace of the Nojima fault, the distribution of aftershocks occurring within 18 h after the earthquake (Nemoto *et al.* 1996), the static displacement determined from triangulation (Hashimoto *et al.* 1996), SAR (synthetic aperture radar) interferograms (Murakami *et al.* 1995), and the particle motion rotations observed very close to the causative fault (Sekiguchi *et al.* 1996). The fault plane is discretized into 310 subfaults, each of which are of length 2.05 km and width 2.05 km. For this size of subfault, the critical hypocentre distance of 10 per cent misfit is about 13.5 km. Most of the station–subfault pairs have larger hypocentre distances than the critical hypocentre distance, and for such pairs only one Green's function on a subfault is enough to give a good approximation of the responses at the station to distributed slips over the subfault. For the station–subfault pairs with smaller distances than the critical hypocentre distance, subdivision of the subfaults is required. Fig. 9 shows how the subfaults should be divided for calculating moving-dislocation element source waveforms

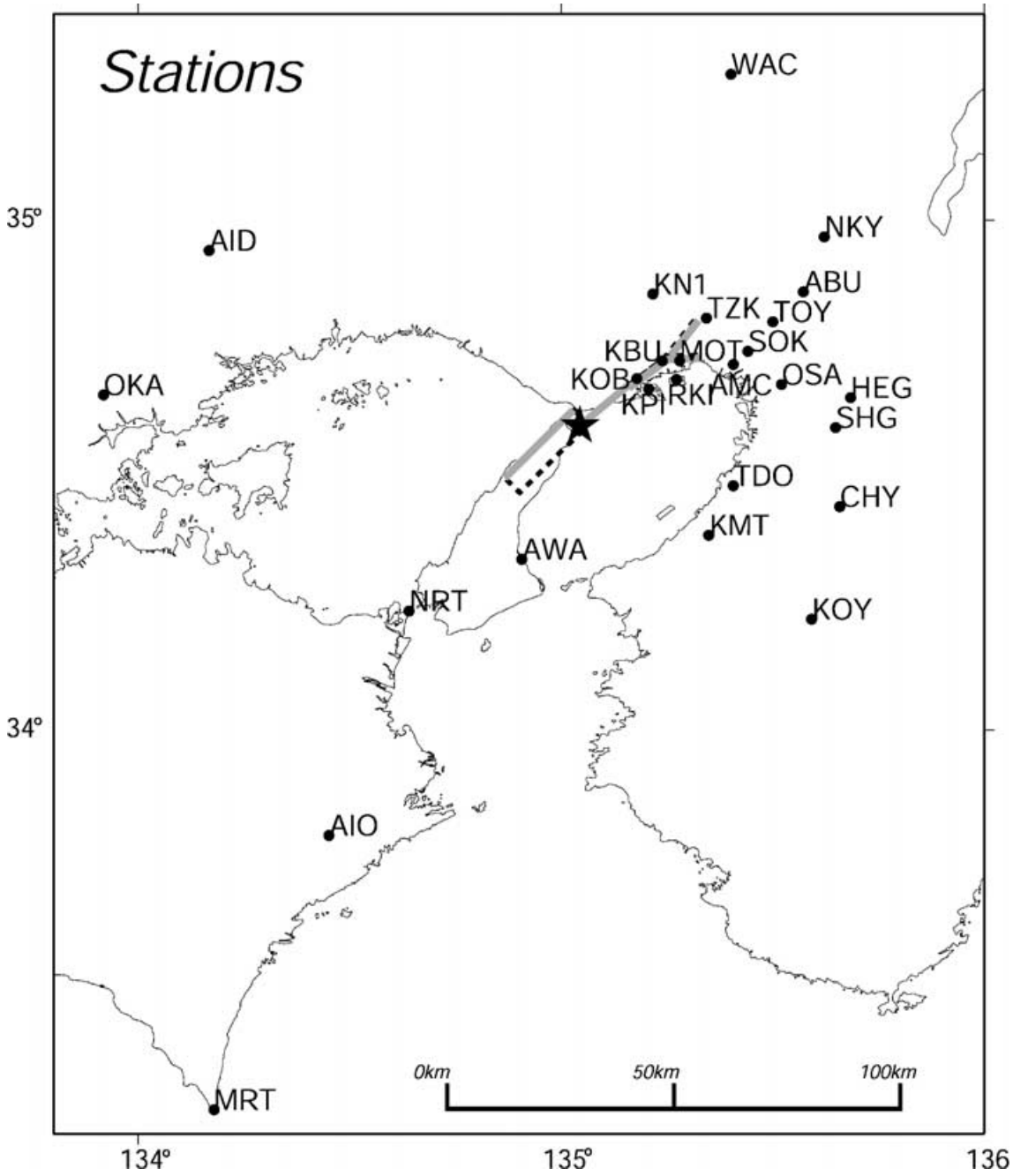

Figure 8. The 25 strong motion stations used in the waveform inversion. The agencies to which these records belong are listed in Table 3.

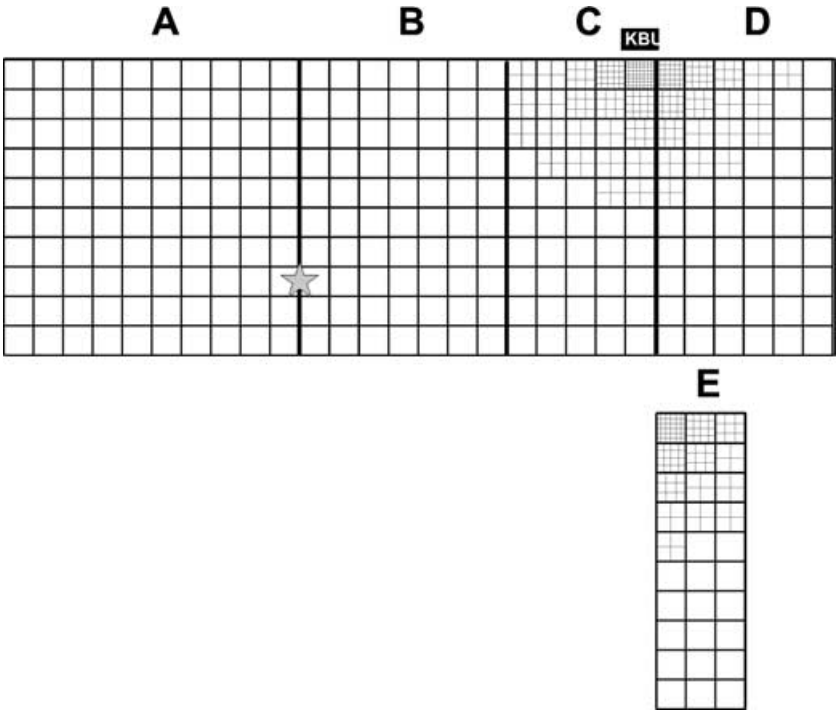

Figure 9. Subdivision of subfaults in order to apply CM for computation of element source waveforms at KBU station (see the map on the left) keeping the approximation error to less than 10 per cent.

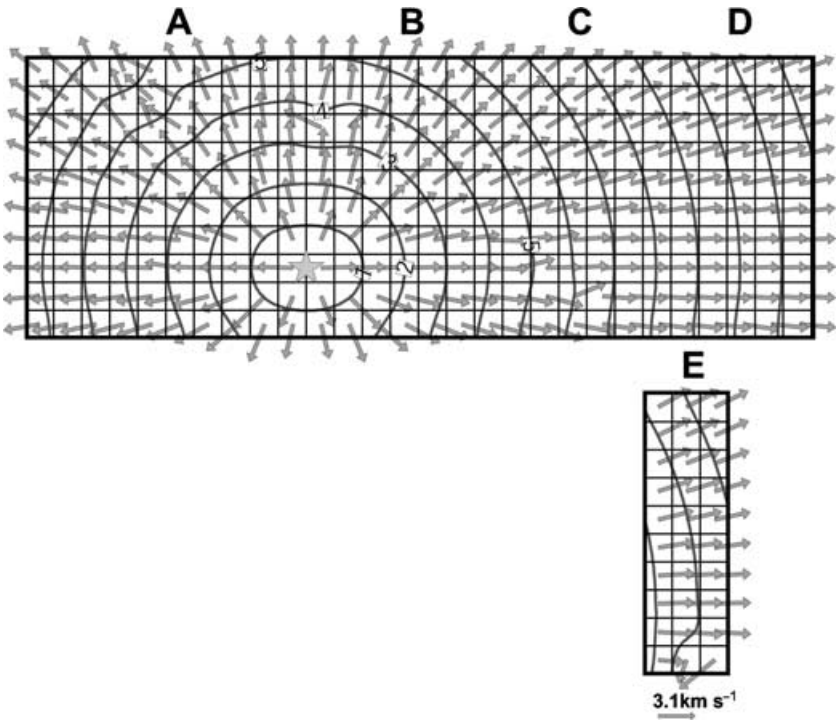

Figure 10. The rupture propagation velocity vectors to be convolved with the Green's functions were calculated from the source model of Sekiguchi *et al.* (2000), assuming that the rupture arrival at each subfault is the time when the moment release exceeded 10 per cent of the total moment release (contour).

at KBU station in order to hold down the plane-wave approximation error to within 10 per cent in misfit. The rupture propagation velocity vectors to be convolved with each Green's function were calculated from the source model of Sekiguchi *et al.* (2000), assuming that the rupture arrival at each subfault is the time when the moment release exceeded 10 per cent of the total moment release (Fig. 10). Fig. 11 shows the element source waveforms from the subfaults at 2 km depth calculated for KBU station, with and without a moving dislocation effect. The waveforms with rupture propagation toward the station have a narrower pulse and drastically

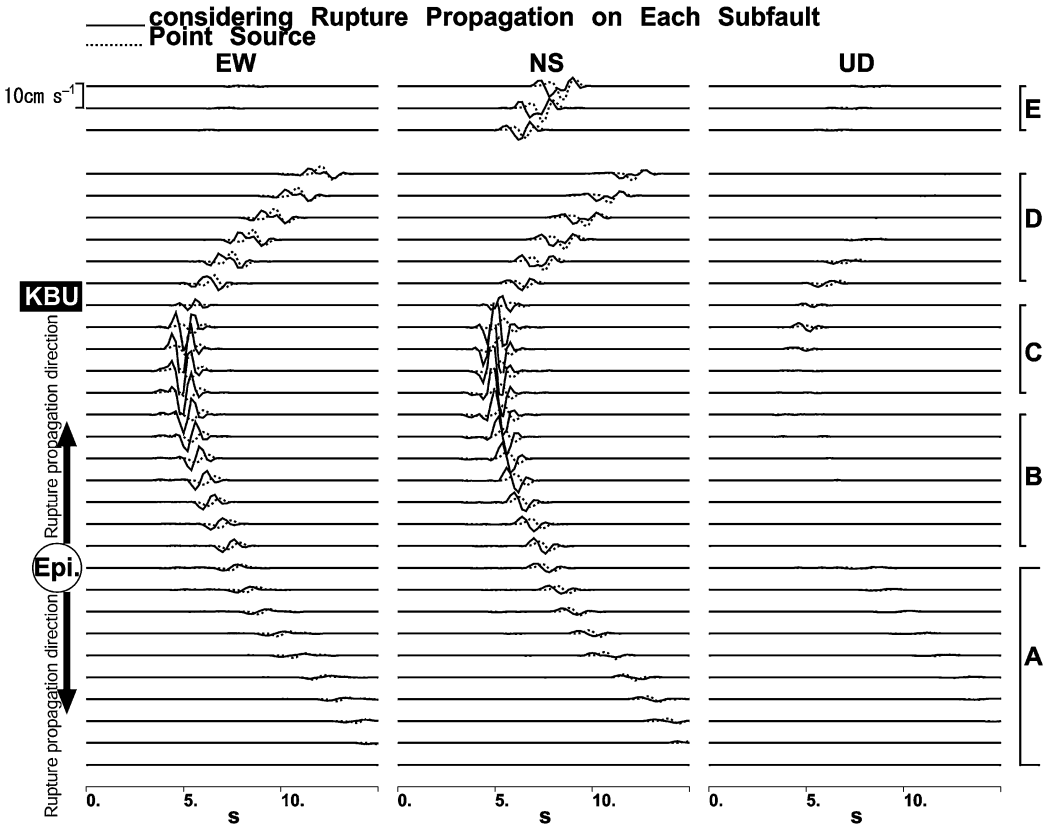

Figure 11. The element source waveforms from subfaults centred at a depth of 2 km with 1.0×10^{17} N m moment and 0.6 rise time calculated for the KBU station, with and without the moving dislocation effect.

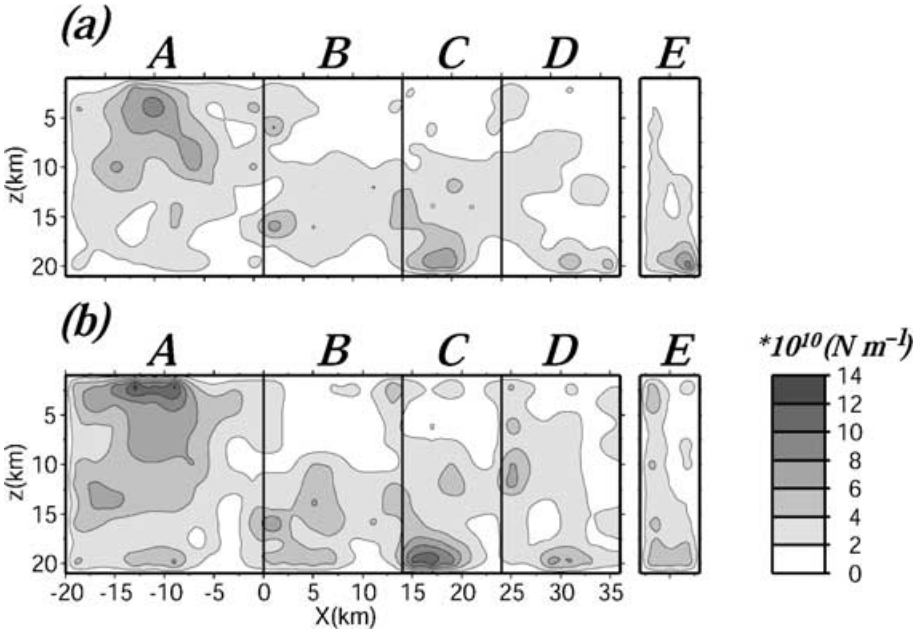

Figure 12. The total moment release density (a) using point-source element waveforms (Sekiguchi *et al.* 2000) and (b) using element source waveforms from a finite moving dislocation using CM.

larger amplitudes than those with rupture propagation against the station. Such differences are not seen in the element source waveforms without considering rupture propagation inside each subfault.

The multitime window linear waveform inversion methodology (Hartzell & Heaton 1983) is applied to estimate the source process. The moment release spatio-temporal distribution is represented by a set of element sources discretized in space and in time. As

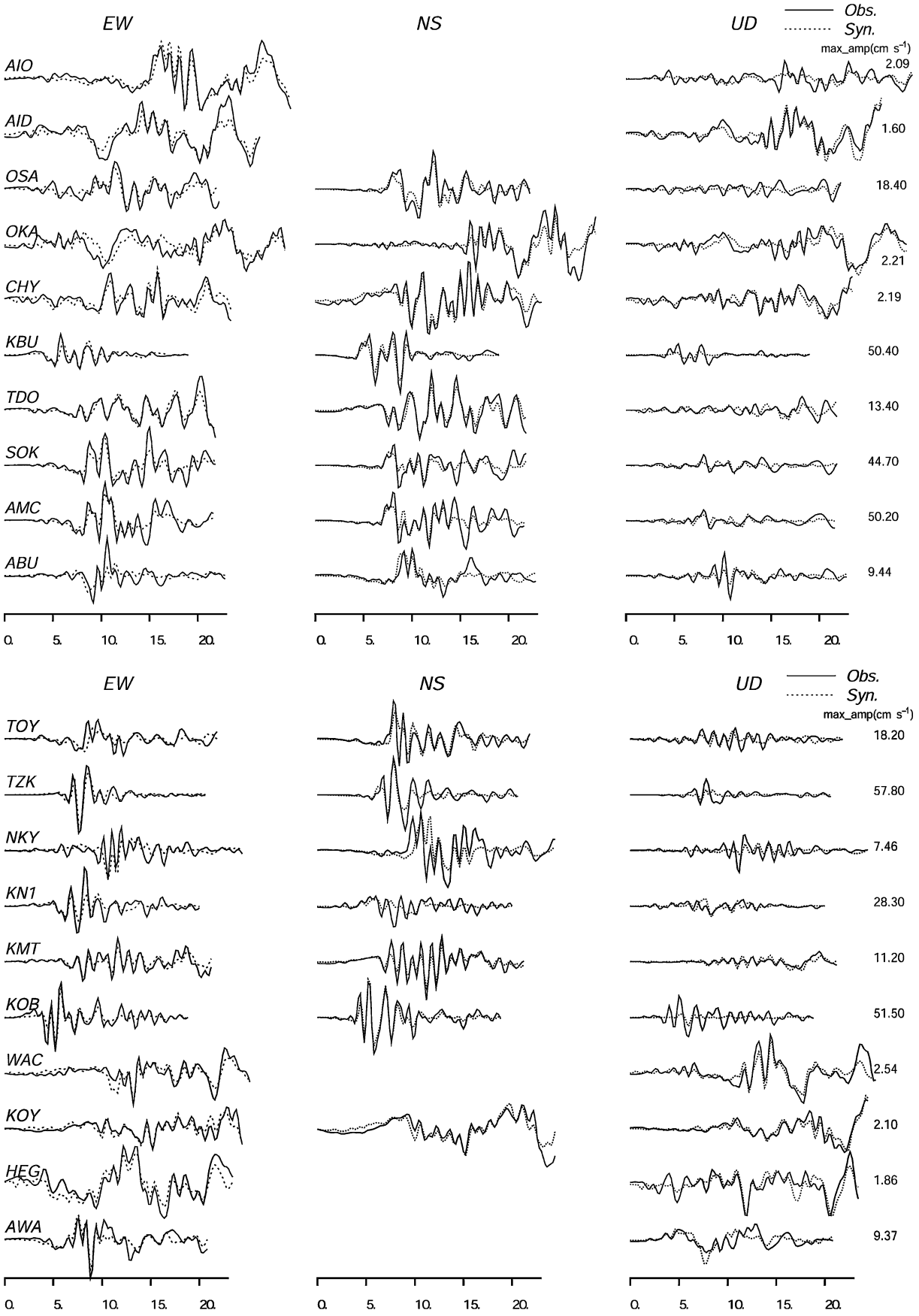

Figure 13. Observed (solid lines) and synthesized (dashed lines) waveforms.

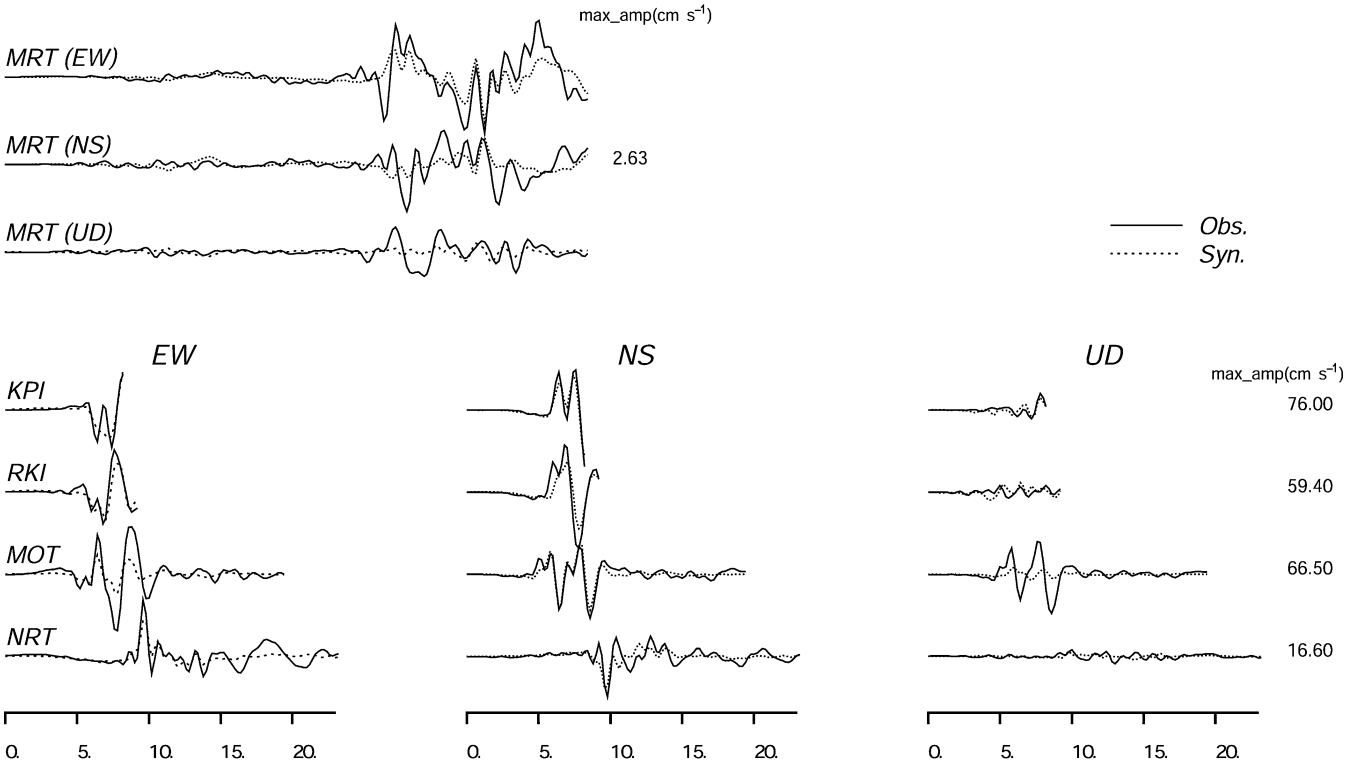

Figure 13. (*Continued*.)

already mentioned, the model fault plane is divided into 2.05 × 2.05 km^2 subfaults located at 2.05 km intervals in strike and dipping directions. The moment release at any point on the model fault plane is represented by the successively activated eight smoothed ramp functions, each of which have a unit duration of 0.6 s at 0.4 s time intervals. The time windows therefore partially overlap each other. The triggering time of the first time window assigned to each subfault is calculated from the source model of Sekiguchi *et al.* (2000). As this inverse problem includes underdetermined model parameters, we impose two constraints; one for restricting the rake angle variation range and the other to smooth out moment release vectors among adjacent model parameters with a strength proportional to the inverse of the distance between model parameters in the spatio-temporal domain (Sekiguchi *et al.* 2000).

3.3 Inversion results

In Fig. 12 the moment release distribution of this study is compared with that obtained using the element source waveforms without the finite moving dislocation effect (after Sekiguchi *et al.* 2000). General features of the moment release distribution obtained using the element source waveforms without the finite moving dislocation effect (Fig. 12a, after Sekiguchi *et al.* 2000) and with the moving dislocation effect (Fig. 12b) are similar to each other. Areas of relatively large moment release (subevents) are at shallow parts on segment A, around the rupture starting point on segment B, at deep parts of segment C, and there is a subevent smaller than the previous three at the deep part on segment E. However, short-wavelength features are different. Fig. 13 shows the comparison between synthesized waveforms using the inverted weights and observed waveforms. A large discrepancy between the observed and the synthesized waveforms is seen at stations MRT, MOT and NKY. It is estimated that the large misfit at station MRT, the furthest station with an epicentre distance of more than 150 km, is a result of the unsatisfactory modelling of the surface waves. At station MOT, the 3-D basin edge is suspected to have deformed the path of the waves. Synthetics at NKY looks shifted compared with the observation due either to the velocity structure model or to mispicking of arrival times. The fit of the waveforms by the present source model is slightly better (about 0.5 per cent of the variance reduction) than that obtained by Sekiguchi *et al.* (2000). The largest improvement is obtained for stations close to the fault; KBU, MOT and KPI.

A positive correlation between the final slip and peak slip velocities is observed (Fig. 14). The relation varies for different segments. On segment B, slip velocities tend to have larger values for certain final slip values than on the other segments.

The distribution of the rise time is shown in Fig. 15. Here, the rise time is defined as the time period where the slip velocity exceed 30 per cent of the maximum value on each subfault. The areas covered with white are of low reliability because their criterion slip velocities defining the rise time are smaller than the estimated error level. The 30 per cent criterion was deduced by: (1) generating a slip time function as proposed by Nakamura & Miyatake (2000) based on a theoretical simulation assuming a local breakdown time corresponding to the observed f_{max}; (2) filtering it in the frequency band in the same way as for the waveform inversion; and (3) comparing the peak and tail slip velocity level during the slip history. This criterion is to prevent the inclusion of low-velocity tails caused by the error in inversion. The rise time varies a lot spatially. At the hypocentre area, the rise time is notably short. The rise time distribution is not correlated with the moment release distribution either, except at a deeper part of segment C.

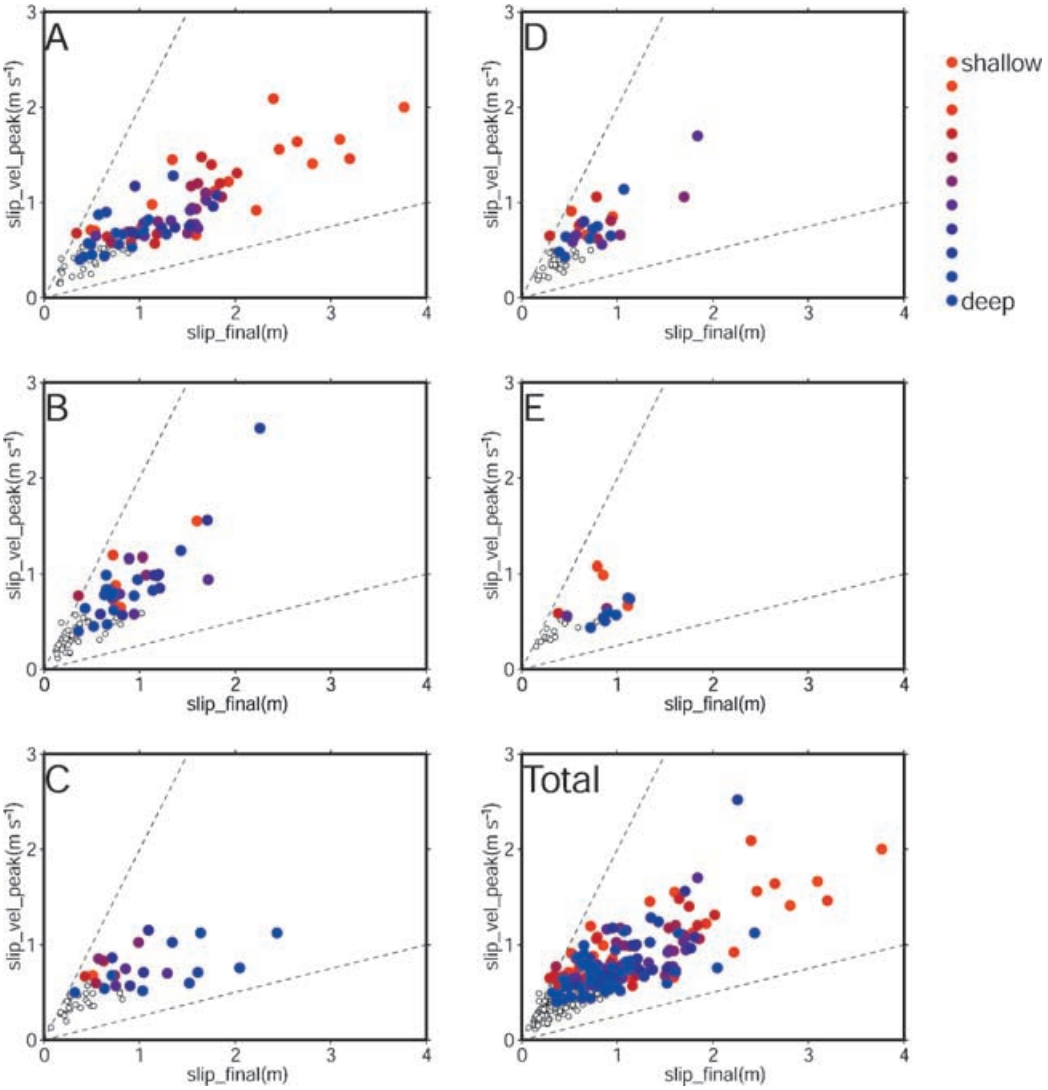

Figure 14. Correlation between the final slip and the peak slip velocity at each subfault.

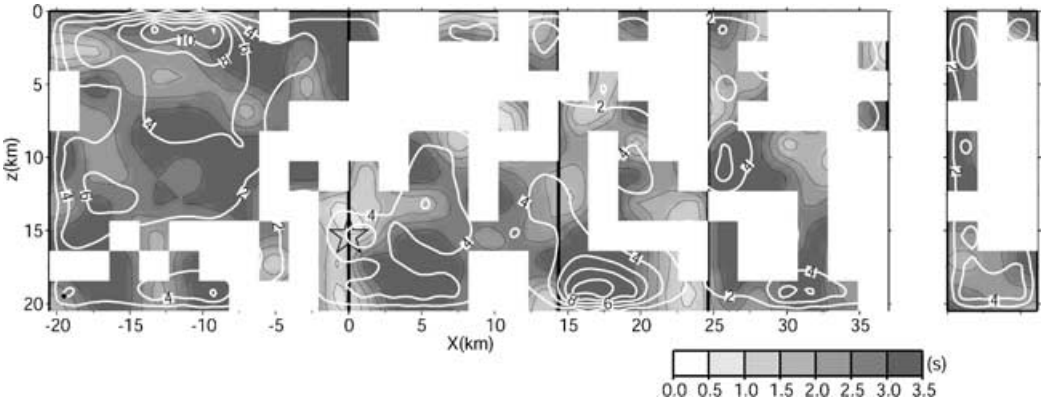

Figure 15. Distribution of the rise time on the fault. The areas covered with white are of low reliability because their criterion slip velocities defining the rise time are smaller than the estimated error level. The white contour lines show the distribution of total moment release density (see Fig. 12).

4 CONCLUSIONS

We have introduced a convolution method (Ben-Menahem 1961) which incorporates the effect of a moving dislocation over a finite area with a point-source synthetic waveform in the calculation of element source waveforms used in the waveform inversion for an earthquake rupture process. Each such element source waves includes the effect of rupture directivity itself. Therefore, the rupture directivity effect on the entire fault area is fully considered in the waveform inversion.

The inverted rupture process by this method has a continuous slip distribution inside the subfaults. The obtained moment release history for each subfault directly reflects the slip time function on the subfault because the rupture propagation effect inside each subfault is separated. It is expected that these slip time functions will give better information concerning the dynamics of the rupture, although contamination of slip time functions resulting from the spatio-temporal smoothing, spatio-temporal discretizing of rupture process and filtering remains. Near-source ground motion simulation using the source model obtained by this method is expected to avoid the problem of artificial, large ground motion near the point sources owing to the use of sparsely distributed point sources.

We applied this convolution method to the computation of element source waveforms in the waveform inversion for the source process of the 1995 Hyogo-ken Nanbu earthquake. The overall characteristics of the moment release distributions are similar between the two inversion results; one inverted with point-source element waveforms and the other with element source waves considering the finite moving dislocation effects inside each subfault. However, short-wavelength features are different between these inversion results. A positive correlation between the final slip and the peak slip velocity are observed.

ACKNOWLEDGMENTS

We thank the organizations who provided us with recordings; the Committee of Earthquake Observation and Research in the Kansai Area; Japan Meteorological Agency; Kansai Electric Power Co. Inc.; the Port and Harbor Research Institute; the Research Center of Earthquake Prediction of the Disaster Prevention Research Institute, Kyoto University; the Research Reactor Institute, Kyoto University; the Public Works Research Institute (1995); Kobe City, Sekisui House Co. Inc.; Matsumuragumi Co. Inc.; and Railway Technical Research Institute (Nakamura *et al.* 1996) (serial no 032). We thank Takao Kagawa for providing us with restored recordings at the KBU and MOT stations. We thank Olivier Coutant who originally coded the program to calculate the Green's function for layered media. We thank Francisco Sanchez-Sesma and Andreas Rietbrock for encouragement and advice. Finally, we show our gratitude to the editor and the two referees, Dr Asya Kaverina and an anonymous one for useful advice that made the point of our paper clearer. We used GMT (Genetic Mapping Tools, version 3.0, Wessel & Smith 1995) to produce the figures. This work was partially supported by a Grant-In-Aid for Scientific Research from the Ministry of Education, Science, Sports, and Culture, Japan.

REFERENCES

Aki, K., 1968. Seismic displacements near a fault, *J. geophys. Res.,* **73**, 5359–5376.

Aki, K. & Richards, P.G., 1980. *Quantitative Seismology,* Vol. 2, p. 804, Freeman, San Francisco, CA.

Ben-Menahem, A., 1961. Radiation of seismic surface-waves from finite moving sources, *Bull. seism. Soc. Am.,* **51**, 401–435.

Ben-Menahem, A., 1962. Radiation of seismic body waves from a finite moving source in the earth, *J. geophys. Res.,* **67**, 345–350.

Ben-Menahem, A. & Singh, S.A., 1981. Seismic waves and sources, p. 1108, Springer-Verlag, New York.

Guatteri, M. & Spudich, P., 2000. What can strong-motion data tell us about slip-weakening fault-friction law?, *Bull. seism. Soc. Am.,* **90**, 98–116.

Hartzell, S.H. & Heaton, T.H., 1983. Inversion of strong ground motion and teleseismic waveform data for the fault rupture history of the 1979 Imperial Valley, California, earthquake, *Bull. seism. Soc. Am.,* **73**, 1553–1583.

Hashimoto, M., Sagiya, T., Tsuji, H., Hatanaka, Y. & Tada, T., 1996. Coseismic displacements of the 1995 Kobe earthquake, *J. Phys. Earth,* **44**, 255–279.

Ishihara, M., Yoshikawa, S., Mitamura, M., Mizuno, K. & Hayashi, T., 1991. 1:125,000 Quaternary geological map of Osaka and adjacent areas, Kinki, Japan, *Urban Kubota,* **30** (in Japanese).

Murakami, M., Fujiwara, S. & Saito, T., 1995. Detection of crustal deformations associated with 1995 Hyogoken-Nanbu earthquake by interferometric SAR, *Current News Geophys. Survey Inst. Japan,* **83**, 24–27.

Nakamura & Miyatake, T., 2000. An approximate expression of slip-velocity time function for simulation of near-field strong ground motion, *Zisin* (in Japanese with English abstract).

Nakamura, Y., Uehan, F. & Inoue, H., 1996. Waveform and its analysis of the 1995 Hyogo-ken Nanbu earthquake (II), *JR Earthquake Information No 23d,*Railway Technical Research Institute (in Japanese).

Nemoto, H., Negishi, H. & Irikura, K., 1997. Re-examination of the hypocenter of the Hyogo-ken Nanbu earthquake, *Zisin (J. seism. Soc. Japan),* **50**, 125–129 (in Japanese).

Nemoto, H., Katao, H., Suzuki, E., Yoshida, Y. & Irikura, K., 1996. The spreading of aftershocks area directly after the 1995 Hyogo-ken Nanbu earthquake, *Programme and Abstracts Seism. Soc. Japan 1996 No 2* (in Japanese).

Sato, R., 1969. Formulations of solutions for earthquake source models and some related problems, *J. Phys. Earth,* **17**, 101–110.

Sekiguchi, H., Irikura, K. & Iwata, T., 2000. Fault geometry in the rupture termination of the 1995 Hyogo-ken Nanbu earthquake, *Bull. seism. Soc. Am.,* **90**, 117–133.

Sekiguchi, H., Irikura, K., Iwata, T., Kakehi, Y. & Hoshiba, M., 1996. Minute locating of faulting beneath Kobe and the waveform inversion of the source process during the 1995 Hyogo-ken Nanbu, Japan, earthquake using strong ground motion records, *J. Phys. Earth,* **44**, 473–487.

Somerville, P., Smith, N.F., Graves, R.W. & Abrahamson, N.A., 1997. Modification of empirical strong ground motion attenuation relations to include the amplitude and duration effects of rupture directivity, *Seism. Res. Lett.,* **68**, 199–222.

Wald, D.J., 1996. Slip history of the 1995 Kobe, Japan, earthquake determined from strong motion, teleseismic, and geodetic data, *J. Phys. Earth,* **44**, 489–503.

Wald, D.J. & Heaton, T.H., 1994. Spatial and temporal distribution of slip for the 1992 Landers, California, earthquake, *Bull. seism. Soc. Am.,* **84**, 668–691.

Wald, D.J., Heaton, T.H. & Hudnut, K.W., 1996. The slip history of the 1994 Northridge, California, earthquake determined from strong-motion, teleseismic, GPS, and leveling data, *Bull. seism. Soc. Am.,* **86**, S49–70.

Wessel, P. & Smith, W.H.F., 1995. New version of the Genetic Mapping Tools released, *EOS, Trans. Am. geophys. Un.,* **76**, 445–446.